Noname manuscript No.
(will be inserted by the editor)

An improved approximation for hydraulic conductivity for pipes of triangular cross-section by asymptotic means

Laura M. Keane · Cameron L. Hall · Iain R. Moyles

Received: date / Accepted: date

Abstract In this paper we explore single phase flow in pores with triangular cross sections at the pore-scale level. We use analytic and asymptotic methods to calculate the hydraulic conductivity in triangular pores, a typical geometry used in network models of porous media flow. We present an analytical formula for hydraulic conductivity based on Poiseuille flow that can be used in network models contrasting the typical geometric approach leading to many different estimations of the hydraulic conductivity. We consider perturbations to an equilateral triangle by changing the length of one of the triangle sides. We look at both small and large triangles in order to capture triangles that are near and far from equilateral. In each case the calculations are compared with numerical solutions and the corresponding network approximations. We show that the analytical solution reduces to a quantitatively justifiable formula and agrees well with the numerical solutions in both the near and far from equilateral cases.

Keywords Porous media flow · triangular flow · hydraulic conductivity · Poiseuille flow · asymptotic analysis

1 Introduction

Flow through porous media is important in a wide range of applications, including water flow through aquifers [1, 2, 3], perfusion of blood [4, 5, 6], and oil extraction [7, 8]. For example, water and gas are often injected to aid in the extraction and recovery of oil from a porous reservoir composed of rock or soil [9, 10]. The petrophysical parameters that drive this flow, such as the hydraulic conductivity, are often estimated by experiments involving core plugs [11], which are samples obtained by drilling into the reservoir. Core plug testing tends to be a time consuming and expensive process so alternative methods for determining parameters involving mathematical modelling and simulation have been developed.

There are two things to model, the porous media and the flow within the porous media. Classically there were two approaches used to model the porous media, the sphere-pack (see [12, 13, 14], and [15]) and the bundle-of-tubes (see [16, 17], and [18]). However, the pore geometry in the sphere-pack was found to be too complex to allow derivations of descriptions of the flow [19], and the bundle-of-tubes model was not found to be very

Laura M. Keane (✉) · Iain R. Moyles
Dept. of Mathematics and Statistics, York University, Toronto, Ontario, Canada.
E-mail: lkeane@yorku.ca

Cameron L. Hall
Dept. of Engineering Mathematics, University of Bristol, Bristol, United Kingdom.

representative of real porous media because it only allows flow in one direction and hence the properties derived from the model did not accurately reflect experimental data. In fact, models of porous media whereby the pores are straight and parallel are seen to be too simple to accurately account for some important features of real porous media. For example, pores of variable cross section connected in series undergo capillary pressure hysteresis during drainage and imbibition cycles due to the connectivity of the pores and this cannot be described using capillary bundles of pores (see [20,21]). Modern work on modelling porous media comprises of models based on percolation theory [22,23], pore scale models such as networks, Lattice Boltzmann and phase field [24], continuum models [25,26], and reconstruction models [27,28]. The recent modelling of porous media attempts to better capture heterogeneity and network connectivity by including pore size distributions [29,20], building in additional state variables such as specific interfacial area [30,31] and percolating versus non-percolating saturation [32,33], and concepts such as accessivity and radius resolved saturation [21].

A range of approaches have been developed for modelling multiphase flow in porous media, including those based on computational fluid dynamics (CFD) [34,35], macroscopic multiphase models [36,37], and models using a network morphology for the pore structure [38,39,40]. CFD approaches are often highly accurate as they involve solving fully non-linear models on non-standard geometries. However, this means that they are computationally expensive and hard to upscale to multi-pore systems. For example, in Van Marcke *et al.* [41], the data sets being studied by the authors would require extensive amounts of memory and computational time in a CFD approach. Conversely, macroscale models consider the soil pores as a single continuum characterised by effective parameters that represent the relationships between macroscopic variables. These parameters depend on the microscale structure but, due to the fact that the geometry of the porous media is removed at the macroscale level, are typically deduced from experiments or simulations. This model simplification reduces the computational complexity making the macroscale approach favourable in a variety of applications (cf. [42,43,44]). However, the results obtained in macroscale models are often sensitive to the choice of empirical function used for the different features of the flow which are being studied [45].

A network modelling approach strikes a balance between the CFD and macroscale model approach. The pores in a real material can be viewed as a set of pore-spaces (nodes) connected by narrow throats (edges) thus preserving some microscale geometry while still allowing for a model-simplified approach. Network models traditionally represent the void space of the porous medium by a two or three dimensional lattice of wide pores connected by narrow throats [40]. There has been a vast amount of work done in modelling multiphase flow on a network, ranging from the pioneering work of Fatt [19], who was the first to model multiphase flow using a network of pores in the 1950s, to more recent developments which focus on dynamic network models such as Tørå *et al.* [11], Al-Gharbi and Blunt [46], and Dahle and Celia [47].

The use of a network model requires that both the pore geometry and flow characteristics be considered. As both fields have a rich history of complex modelling, often a compromise in simplicity is made for each case. Many networks want to consider multi-phase flow which requires the allowance of a contact angle in the pore geometry. For this reason, pores of triangular cross-section are preferred (see [11,46], and [48]). To simplify the fluid modelling, these authors consider the fluid to follow Poiseuille flow through a cylinder, and use the triangular geometry to estimate appropriate parameters. The architecture of the network structure removes the microscale impact of geometry on the global flow, but the geometry is retained in the fluid characteristics and that is where we will focus our attention. The main downfall of these geometric methods is the fact that the hydraulic conductivity, a property of the porous medium which depends on the flow profile, is determined purely from the pore geometry, without any information about the flow. Furthermore, because the hydraulic conductivity depends on the specific geometry parameters, solutions may have to be recomputed for different-sized pores of the same geometry.

We consider a more detailed model of fluid flow that appropriately captures the triangular geometry and extracts the hydraulic conductivity as a consequence of the model of fluid flow and not solely geometry. We emphasize that our goal is not to criticize the main assumptions that go into simplifying the modelling of pore geometry and flow for network models, but to provide a more accurate formulation of the conductivity without sacrificing computational speed due to the other simplifications. We focus on an analytical formulation of the conductivity so that it is computationally equivalent to the geometric formula used. Analytical solutions for slow viscous flow through equilateral triangular tubes has long been considered with the first velocity profile derived by Boussinesq [49]. An analytical solution was extended to isosceles triangles by Proudman [50]. Sparrow [51] developed a point matching technique which was used to derive an analytical expression for flow in an isosceles duct, similar techniques were used by Tamayol and Bahrami [52] in their work on non-circular cross sections. Shah [53] used a least squares matching technique to study flow in cross sections such as an isosceles triangle and Navardi *et al.* [54] derived an analytical description of flow in distorted triangular shapes. An overview of the work done on modelling flow properties in triangular cross sections can be found in Shah and London [55] and Kumar *et al.* [56]. However, the corner angles in pores are typically nonuniform and flow is best modelled using scalene triangles [57].

Fully detailed flow in scalene triangle requires numerical computations which diminishes the advantages of a simplified model approach such as networks. For example, flow in arbitrary triangles is studied by authors such as Nakamura *et al.* [58] and Abdel-Wahed and Attia [59] using finite difference techniques. Instead we will consider an asymptotic approach that captures a class of scalene triangles as those near and far from equilateral.

While the intent of triangular pores is to capture contact angles in multi-phase flow, we will focus on single-phase flow to simplify the model. This is an appropriate approximation to use in oil extraction from reservoirs with oil saturation. We will demonstrate that our technique remains simple enough to implement in network models while performing better than alternative geometric methods which are currently used [48].

This paper is presented as follows: In Section 2 we derive the flow model and assumptions that will be used in our analysis. This leads to Section 3 where we set up our model geometry and then carry out the asymptotic analysis to compute the velocity profiles in the triangular pores. In Section 3.1 we consider a small perturbation to an equilateral triangle while in Section 3.2 we consider a large perturbation. Having computed the velocity profiles, we calculate the analytical expressions for the hydraulic conductivity in Section 4 which depend on one parameter related to the size of the triangle and does not require multiple simulations of flow. In Section 4.3 we compare our expression for hydraulic conductivity to one that is numerically computed as well as geometric conductivity formulae used by Tørå *et al.* [11] and Al-Gharbi and Blunt [46] in network models. We compare the results for triangles of a variety of size and show that we generally outperform geometric estimates. Finally, Section 5 summarises the work carried out in this paper and outlines possible directions for future work.

2 Modelling fluid flow

We choose our axes so that both a triangular pipe of uniform cross-section and the flow are oriented in the $z-$direction as shown in Figure 1 and consider a single fluid of constant density ρ moving with velocity $\mathbf{v} = (v_x, v_y, v_z)$, which can vary though time and space. Conservation of mass and momentum in the incompressible limit yield the Navier–Stokes equations,

$$\nabla \cdot \mathbf{v} = 0, \tag{1a}$$

$$\frac{\partial \mathbf{v}}{\partial t} + (\mathbf{v} \cdot \nabla)\,\mathbf{v} = -\frac{1}{\rho}\nabla p + \frac{\mu}{\rho}\nabla^2 \mathbf{v}, \tag{1b}$$

subject to no-slip ($\mathbf{v} = \mathbf{0}$) on the boundary, where t is time and ∇ is the gradient operator $\nabla = \mathbf{e}_i \frac{\partial}{\partial x_i}$ with $\mathbf{e}_i$ as the i^{th} unit vector. Furthermore, we denote p to be the fluid pressure (or piezometric head) and μ the fluid dynamic viscosity (assumed constant). We will neglect the effects of body forces without loss of generality, and assume that the pressure has a constant gradient in the direction of flow. We non dimensionalise (1) with the following scales,

$$x \sim l x', \qquad \mathbf{v} \sim V \mathbf{v}', \qquad t \sim \frac{l}{V} t', \qquad p \sim \Delta p p',$$

where l is a characteristic length scale, V a velocity scale and Δp a scale for the variation in pressure. We will choose the velocity scale, V, so that $V = -\frac{\Delta p l}{\mu}$ allowing the flow to be dominantly driven by a pressure gradient. The momentum equation becomes (after dropping the primes),

$$\mathrm{Re}\left(\frac{\partial \mathbf{v}}{\partial t} + (\mathbf{v} \cdot \nabla)\,\mathbf{v}\right) = \nabla p + \nabla^2 \mathbf{v}, \tag{2}$$

where the Reynolds number, $\mathrm{Re} = \frac{\rho l V}{\mu}$, represents the ratio of inertial to viscous forces. It is typically used to separate laminar and turbulent flow where the former is characterised by smooth, constant fluid motion and occurs when $\mathrm{Re} \ll 1$, while the latter produces fluid instabilities, such as a transition to turbulence, and is associated with $\mathrm{Re} \gg 1$. We will focus attention on the laminar case, which reduces the Navier–Stokes equations to the Stokes flow equations. We assume the flow is of Poiseueille type, i.e., it is steady and well developed so that the transverse velocity gradients are zero. It then follows that the pressure is linear in z, reducing the momentum equation to

$$\frac{\partial^2 v_z}{\partial x^2} + \frac{\partial^2 v_z}{\partial y^2} = -1, \tag{3}$$

where $v_z = v_z(x,y)$ due to the incompressibility condition.

3 Single phase flow in triangular pores

3.1 Small perturbation to equilateral triangle

Having already non-dimensionalized, we consider an equilateral triangle of side length 1, with its axis coincident with the Cartesian $z-$axis. We consider a perturbation to the equilateral triangle as shown in Figure 2 where the corner at $\left(\frac{1}{2}, 0\right)$ is extended by ε in the positive x-direction, for some $\varepsilon > 0$. We also orientate the triangle so that the vertex C lies on the $y-$axis.

We seek a solution to (3) which also satisfies the no-slip condition on the boundary. We define a function $W(x,y)$ given by

$$W = y\left(y - \sqrt{3}\left(x + \frac{1}{2}\right)\right)\left(y + \sqrt{3}\left(\frac{x}{1+2\varepsilon} - \frac{1}{2}\right)\right), \tag{4}$$

so that $W = 0$ along the pipe walls. We want to solve a problem of the form

$$\nabla^2 v = -1 \text{ subject to } v = 0 \text{ on } W = 0, \tag{5}$$

and do this via a regular expansion to (4) around $\varepsilon = 0$ of the form $W = W_0 + \varepsilon W_1 + \mathscr{O}\left(\varepsilon^2\right)$ which yields

$$W_0 = y\left(y - y_1\right)\left(y - y_2\right), \tag{6a}$$

$$W_1 = -2\sqrt{3}xy\left(y - y_1\right), \tag{6b}$$

where $y_1 = \sqrt{3}\left(x + \frac{1}{2}\right)$ and $y_2 = -\sqrt{3}\left(x - \frac{1}{2}\right)$. Similar to W, we pose an expansion $v = v_0 + \varepsilon v_1$, and substitute into (5). At $\mathscr{O}(1)$ we have

$$\nabla^2 v_0 = -1 \tag{7a}$$

subject to

$$v_0(x,0) = 0, \qquad v_0(x, y_1(x)) = 0, \qquad v_0(x, y_2(x)) = 0 \tag{7b}$$

while at $\mathscr{O}(\varepsilon)$ we have

$$\nabla^2 v_1 = 0 \tag{8a}$$

subject to

$$v_1(x,0) = 0, \qquad v_1(x, y_1(x)) = 0, \qquad v_1(x, y_2(x)) = -2\sqrt{3}x\left(\left.\frac{\partial v_0}{\partial y}\right|_{y=y_2}\right). \tag{8b}$$

We note that this third boundary condition in (8b) resembles that of a slip condition on the boundary. Problems with symmetric slip conditions have been studied by Lekner [60].

We take this approach as we wish to exploit the fact that solutions for velocity profiles in an equilateral triangle domain, which the $\mathscr{O}(1)$ problem satisfy, are known. Following the approach taken by others, such as Lekner [61], the equilateral triangle problem (7) can be solved by taking an ansatz of the form $v_0 = u_0 W_0$ for some function $u_0(x,y)$. We do this for two reasons. Firstly, the boundary condition $v_0 = 0$ on the pipe walls is automatically satisfied; secondly, the fact that W_0, as defined in (6a), is cubic in y and quadratic in x means that it simplifies greatly under the Laplace operator. Assuming $v_0 = u_0 W_0$, (7a) becomes

$$\left(\frac{\partial^2 u_0}{\partial x^2} + \frac{\partial^2 u_0}{\partial y^2}\right) W_0 + 2\left(\frac{\partial u_0}{\partial x}\frac{\partial W_0}{\partial x} + \frac{\partial u_0}{\partial y}\frac{\partial W_0}{\partial y}\right) - 2\sqrt{3}u_0 = -1, \tag{9}$$

which has constant solution, $u_0 = \frac{1}{2\sqrt{3}}$, and hence our solution for v_0 takes the form

$$v_0 = \frac{1}{2\sqrt{3}} W_0. \tag{10}$$

Contours of constant v_0 are plotted in Figure 3. The contours are triangular at the pipe walls but become circular towards the centre of the pipe. This indicates that, far enough away from the pipe walls, the velocity profile is like that of a cylindrical tube. This is important to note as many of the related network models for porous media flow assume cylindrical Poiseuille flow in their computations. Now, it remains to solve the $\mathscr{O}(\varepsilon)$ problem, (8). Given v_0 we can compute $\frac{\partial v_0}{\partial y}$,

$$\frac{\partial v_0}{\partial y} = \left(\left(y - y_1\right)\left(y - y_2\right) + y\left(y - y_1\right) + y\left(y - y_2\right)\right) u_0. \tag{11}$$

Making the observation that

$$\begin{aligned}\left(\left.\frac{\partial v_0}{\partial y}\right|_{y=y_2}\right) &= \left(y(y - y_1)\right) u_0 \\ &= -\frac{u_0}{2\sqrt{3}x} W_1,\end{aligned} \tag{12}$$

then the third condition in (8b) becomes

$$v_1(x, y_2) = u_0 W_1. \tag{13}$$

We therefore seek a solution for v_1 of the form

$$v_1 = u_0 W_1 + u_0 \hat{v} \tag{14}$$

for some function $\hat{v}$. This expansion works because $W_1(x,0) = W_1(x,y_1) = 0$ as well. Substituting (14) into (8b) with the third condition given by (13) yields the new problem

$$\nabla^2 \hat{v} = -\nabla^2 W_1 \qquad \text{with} \qquad \hat{v} = 0 \qquad \text{on} \qquad W_0. \tag{15}$$

We have reduced the homogeneous problem on a perturbed geometry to an inhomogeneous problem on the unperturbed triangle geometry. Instinctively, we would solve (15) using a separation of variables approach, however this is not possible in Cartesian coordinates when the boundaries are not at $x =$ constant or $y =$ constant. Alternatively, one could solve the original problem (3) on any triangular domain using conformal mapping techniques [62,63]. This solution approach involves transforming the triangular domain to the upper half plane and results in elliptic functions, which, in practice require numerical computations to evaluate and therefore are not immediately beneficial compared to a numerical solution to the partial differential equation. The integrals could be expanded asymptotically, but it is not clear this is better than the asymptotic approximation of the differential equation directly. Instead, we write the problem in triangular coordinates. Transforming the problem to one in the triangular coordinate system will allow a separation of variables approach as the boundaries of the triangle in this system will be constant (see Appendix A). The orthogonal coordinates which we will work with in this new coordinate system are given by ξ and η, where $\xi = r_{\text{inc}} - y = u$ and $\eta = \sqrt{3}x = v - w$ as shown in Figure 4. Here $r_{\text{inc}} = \frac{\sqrt{3}}{6}$ is the radius of the inscribed circle of the triangle. Writing (15) in triangular coordinates

$$\hat{\nabla}^2 \hat{v} = 4\eta + 12\xi - 12 r_{\text{inc}} \qquad \text{with} \qquad \hat{v} = 0 \qquad \text{on} \qquad W_0, \tag{16}$$

where $\hat{\nabla}$ is the Laplace operator in the triangular coordinate system given by

$$\hat{\nabla}^2 = \frac{\partial^2}{\partial \xi^2} + 3\frac{\partial^2}{\partial \eta^2}. \tag{17}$$

Since (16) is an inhomogeneous problem we will consider an eigenfunction expansion with eigenfunctions

$$\hat{\nabla}^2 \phi = -\lambda^2 \phi \qquad \text{with} \qquad \phi = 0 \qquad \text{on} \qquad W_0. \tag{18}$$

We solve (18) by seeking a separable solution of the form $\phi(\xi,\eta) = f(\xi)g(\eta)$ and find that both f and g are simple harmonic oscillators. In order to satisfy the boundary conditions, $\phi = 0$ on the boundaries of the triangle as described in triangular coordinates, we choose a basis for ϕ by considering separately the even and odd functions of ϕ in η and ξ, both of which will contribute to our solution. This leads us to the following additive solutions,

$$\begin{aligned}
\phi_e^{mn} = {} & \sin\left(\frac{l\pi}{3r_{\text{inc}}}(\xi + 2r_{\text{inc}})\right)\cos\left(\frac{(m-n)\pi}{9r_{\text{inc}}}\eta\right) + \sin\left(\frac{m\pi}{3r_{\text{inc}}}(\xi + 2r_{\text{inc}})\right)\cos\left(\frac{(n-l)\pi}{9r_{\text{inc}}}\eta\right) \\
& + \sin\left(\frac{n\pi}{3r_{\text{inc}}}(\xi + 2r_{\text{inc}})\right)\cos\left(\frac{(l-m)\pi}{9r_{\text{inc}}}\eta\right),
\end{aligned} \tag{19a}$$

$$\begin{aligned}
\phi_o^{mn} = {} & \sin\left(\frac{l\pi}{3r_{\text{inc}}}(\xi + 2r_{\text{inc}})\right)\sin\left(\frac{(m-n)\pi}{9r_{\text{inc}}}\eta\right) + \sin\left(\frac{m\pi}{3r_{\text{inc}}}(\xi + 2r_{\text{inc}})\right)\sin\left(\frac{(n-l)\pi}{9r_{\text{inc}}}\eta\right) \\
& + \sin\left(\frac{n\pi}{3r_{\text{inc}}}(\xi + 2r_{\text{inc}})\right)\sin\left(\frac{(l-m)\pi}{9r_{\text{inc}}}\eta\right),
\end{aligned} \tag{19b}$$

where $m,n \in \mathbb{N},\ n \geq m$ for $\phi_e,\ n > m$ for $\phi_o,\ l = -m-n$, and $\phi_o,\ \phi_e$ refer to the functions being odd or even in η respectively. We note that the eigenfunctions form a complete and orthogonal set (see [64] and [65]). The corresponding eigenvalue for this solution is

$$\lambda_{mn}^2 = \frac{4\pi^2}{27r_{\text{inc}}^2}(m^2+mn+n^2). \tag{20}$$

Details of the calculations performed are described in Appendix A.
We decompose (16) as $\hat{v} = 4\hat{v_\eta} + 12\hat{v_\xi} - 12r_{\text{inc}}\hat{v_r}$, where

$$\hat{\nabla}^2\hat{v_\eta} = \eta, \tag{21a}$$

$$\hat{\nabla}^2\hat{v_\xi} = \xi, \tag{21b}$$

$$\hat{\nabla}^2\hat{v_r} = 1, \tag{21c}$$

so that (16) is satisfied. To solve (21c) we recall that the solution to the $\mathscr{O}(1)$ problem, $\nabla^2 v_0 = -1$, is $v_0 = u_0 W_0$ so it follows that

$$\hat{v_r} = -u_0 W_0. \tag{22}$$

We also note that $12r_{\text{inc}} = \frac{1}{u_0}$, so we have that $-12r_{\text{inc}}\hat{v_r} = W_0$. To solve (21a) and (21b) we must expand $\hat{v_\eta}$ and $\hat{v_\xi}$ as eigenfunction series. Suppose that $\hat{\nabla}^2\hat{v} = h$ for some arbitrary h on the left hand side. Then, using (18) and expanding

$$\hat{v} = \sum_{m=1}^{\infty}\sum_{n=m}^{\infty} B_e^{mn}\phi_e^{mn} + \sum_{m=1}^{\infty}\sum_{n=m+1}^{\infty} B_o^{mn}\phi_o^{mn},$$

we deduce that

$$B_i^{mn} = -\frac{1}{\lambda_{mn}^2}\frac{\int_T \phi_i^{mn} h \,\mathrm{d}T}{\int_T (\phi_i^{mn})^2\,\mathrm{d}T} \tag{23}$$

where λ_{mn} is the eigenvalue corresponding to the eigenfunction ϕ_i^{mn}, given by (19). These B_i^{mn} coefficients can be computed analytically. Here we have used Green's identity and Gauss' Divergence Theorem, with the inner product in the unperturbed triangular coordinate system given by

$$\begin{aligned} \iint_T f(x,y)\,\mathrm{d}T &= 2\int_0^{\frac{1}{2}}\int_0^{-\sqrt{3}\left(x-\frac{1}{2}\right)} f(x,y)\,\mathrm{d}x\,\mathrm{d}y \\ &= \frac{1}{\sqrt{3}}\int_{-2r_{\text{inc}}}^{r_{\text{inc}}}\int_{-\xi-2r_{\text{inc}}}^{\xi+2r_{\text{inc}}} f(\xi,\eta)\,\mathrm{d}\eta\,\mathrm{d}\xi \\ &= \iint_{\hat{T}} f(\xi,\eta)\,\mathrm{d}\hat{T} \end{aligned} \tag{24}$$

for a function $f(x,y)$, with T representing the equilateral domain in Cartesian coordinates and $\hat{T}$ representing the same domain in triangular coordinates.

We are now in a position to solve (21a) and (21b). For (21a) we note that η is odd and that the inner product in the triangular coordinate system involves a symmetric integral over η, and thus we only need to consider the odd eigenfunctions. Thus, the solution to (21a) is

$$\hat{v_\eta} = \sum_{m=1}^{\infty}\sum_{n=m+1}^{\infty} B_\eta^{mn}\phi_o^{mn}, \qquad B_\eta^{mn} = -\frac{\int_{\hat{T}} \phi_o^{mn}\eta\,\mathrm{d}\hat{T}}{\lambda_{mn}^2\int_{\hat{T}}(\phi_o^{mn})^2\,\mathrm{d}\hat{T}}. \tag{25}$$

The calculation for (21b) is carried out in the same manner. For the eigenfunction expansion of ξ we note that the ϕ_o terms will drop out (ϕ_o is odd in η and so will again drop out due to the symmetry in the η integral), and so the solution to (21b) is given by

$$\hat{v_\xi} = \sum_{m=1}^{\infty}\sum_{n=m}^{\infty} B_\xi^{mn}\phi_e^{mn}, \qquad B_\xi^{mn} = -\frac{\int_{\hat{T}} \phi_e^{mn}\xi\,\mathrm{d}\hat{T}}{\lambda_{mn}^2\int_{\hat{T}}(\phi_e^{mn})^2\,\mathrm{d}\hat{T}}. \tag{26}$$

Matlab (version R2018b) was used to numerically compute the solution to (3) on this geometry where we use a Finite Element Method (FEM) mesh with a maximum edge length of 2.5×10^{-3}. For each value of ε we computed that the number of triangles used in the mesh is $\approx 2.8\times10^{-6}$ multiplied by the area of the full triangle. In other words, in order to ensure consistent numerical results were obtained, the ratio of the area of the triangle to the number of triangles used in the mesh was kept at this number, with the first two significant figures being the same each time. This ratio, along with the maximum edge length, also indicate that the error of the numerical solution is smaller than the asymptotic error up to $\varepsilon\sim10^{-3}$. We truncate the sums at $N=25,\ M=24$ so that $\max(\lambda^2)=10^4$, also consistent with the asymptotic error.

To observe the agreement with the separation of variables solution, we subtract the u_0W_0 and u_0W_1 terms from both the analytical and numerical solutions and plot the $L2-$norm of the results for various values of ε, which are shown in Figure 5. As observed in Figure 5 the error decreases as we decrease ε indicating that the separation of variables in triangular coordinates matches the numerical computations very well. A stepsize of $h=0.005$ in both x and y was used in interpolating the numerical solution from the triangular mesh to a rectangular grid.

3.2 Large perturbation to the equilateral triangle

We now consider modelling a large perturbation to the equilateral triangle by perturbing the right vertex by ε for $\varepsilon\gg1$ so that the triangle can be approximated by an infinite wedge. In order to carry out the asymptotics in this case we introduce $\delta=\varepsilon^{-1}$, where δ is our small parameter in this large perturbation problem. We will derive an analytic expression for the velocity profile in an infinite wedge and we will show that this is in good agreement with the numerical solution in this perturbed triangle.

Consider the geometry of an isosceles wedge-shaped duct of angle 2α as shown in Figure 6, where (r, ϕ, z) represent the radius, azimuthal angle and in-field depth of cylindrical polar coordinates. Flow in an isosceles triangular duct was studied by Sparrow [51] while isosceles and equilateral wedges were considered by Bazant [66]. We use a similar solution approach here to determine the velocity profile of the infinite wedge. Writing Poiseuille flow in cylindrical polar co-ordinates with $v_z=v_z(r,\theta)$,

$$\frac{\partial^2 v_z}{\partial r^2}+\frac{1}{r}\frac{\partial v_z}{\partial r}+\frac{1}{r^2}\frac{\partial^2 v_z}{\partial\phi^2}=-1. \tag{27}$$

For the duct-wedge geometry we want to solve (27) subject to the boundary conditions $v_z=0$ on the duct boundaries ($\phi=\pm\alpha$), and v_z finite at $r=0$. An application of separation of variables leads to the solution

$$v_z=\frac{1}{4}\left(r^2\left(\frac{\cos2\phi}{\cos2\alpha}-1\right)+\sum_{n=1}^{\infty}A_n r^{\frac{(2n-1)\pi}{2\alpha}}\cos\left(\frac{(2n-1)\pi\phi}{2\alpha}\right)\right). \tag{28}$$

The prescription for A_n comes from matching to a weak boundary layer at the other side of the triangle where $v_z=0$. For the large triangle we can determine the wedge angle to be

$$\alpha=\frac{1}{2}\arcsin\left(\frac{\sqrt{3}\delta}{2\sqrt{1+\delta+\delta^2}}\right)\ll1, \tag{29}$$

which suggests that we scale $\phi=\alpha\theta$ with $-1<\theta<1$. Inspection of (28) in this limit requires $A_n\to0$ for sensible matching. Expanding v_z in a Taylor series around $\delta=0$ furnishes the following asymptotic solution,

$$v_z=\frac{3r^2}{32}\left(\left(1-\theta^2\right)\left(\delta^2-\delta^3\right)\right)+\mathscr{O}\left(\delta^4\right). \tag{30}$$

3.2.1 Numerics

In order to get around the issue of the size of numerical computations required for this large triangle, we consider the equivalent numerical problem in a scaled geometry, as shown in Figure 7. We scale r and the sides of this large triangle by δ^{-1}, to a similar but asymptotically smaller triangle, to improve the reliability of numerical solutions. Numerical solutions for the velocity profile in this large perturbed triangle are computed using Matlab. In this case we use an FEM mesh with a maximum edge length of 5×10^{-4}. The maximum edge length value is smaller than that used in the small perturbation case due to the asymptotically smaller area, and is necessary for the numerics to be sufficiently resolved. In this case, for each value of δ, the number of triangles used in the mesh is $\approx 1.1 \times 10^{-7}$ times the area of the full triangle.

In order to compare the velocity profiles for the numerical and wedge hydraulic conductivities we perform transformations from cylindrical coordinates to Cartesian coordinates so that the wedge is orientated in the same way as our original triangle, and so that the wedge velocity is computed on points corresponding to that of the triangle. Here, the stepsize for the interpolation grid in $x-y$ is taken so that we have 500 points in y and $h = 0.002$ so that we have about 500 points in x. The additional points are needed to improve the numerical reliability and to resolve the small boundary layer that arises on the edge opposite the angle 2α. Figure 8 shows the difference between the numerical solution for the velocity of the large perturbed triangle and the wedge velocity, where we have taken $\varepsilon = \delta^{-1} = 10$. This figure shows that these two solutions are in excellent agreement, with the only difference at the far boundary of the triangle. This is due to the fact that the numerical solution must satisfy the zero condition on this boundary, but the wedge does not. Fortunately, this boundary layer is of negligible width and does not affect our solution as demonstrated in Figure 9 where we see a convergence between our asymptotic solution and the numerical one accurate to $\mathscr{O}\left(\varepsilon^{-4}\right)$.

4 Fluid hydraulic conductivities for single phase flow

In simulating porous media the hydraulic conductivity plays a vital role. The hydraulic conductivity is defined as a measure of how easily fluid can move through the pore space and is important for understanding pore pressures as well as a useful tool for comparing different approaches to porous flow. In practice, accurate estimates of the conductivity and pressure are important. For flow in pipes, both overestimations and underestimations of the fluid pressure can have inconvenient implications, such as pipe erosion and leaking [67].

The hydraulic conductivity per unit length, K, which is also referred to as conductance [11,46], is defined in terms of the volume flux, Q and the pressure difference, $\varDelta p$ [68] by the formula

$$Q = K\varDelta p, \tag{31}$$

where Q is defined to be

$$Q = \iint_T \mathbf{v} \cdot \mathrm{d}T, \tag{32}$$

with T being the cross sectional area of the pipe. The conductivity is an intrinsic property of porous media that depends on the pressure field and the velocity field. Since we know the velocity profiles of the near equilateral and far from equilateral scalene triangle geometries, we can proceed with computing the analytical conductivity in these geometries using the results obtained in Sections 3.1 and 3.2. This is in contrast to geometric methods that have been used in approximations of the conductivity by network models.

4.1 Conductivity formulae

4.1.1 Derivation of analytic formula

The network models present their results for hydraulic conductivity in terms of $G = \mu LK$. For the analytic formula we then consider (31), the assumption of a linear pressure drop $\left(\frac{\Delta p}{L} = -\frac{\mathrm{d}p}{\mathrm{d}z}\right)$ and the relationship $G = \mu LK$ giving the analytic formula for the hydraulic conductivity by the following relationship

$$Q = -\frac{1}{\mu}\frac{\mathrm{d}p}{\mathrm{d}z}G \tag{33}$$

Since we have scaled the velocity with $-l^2 \frac{1}{\mu}\frac{\mathrm{d}p}{\mathrm{d}z}$, the natural scale for the flux will be

$$Q \sim -l^4 \frac{1}{\mu}\frac{\mathrm{d}p}{\mathrm{d}z}Q',$$

resulting in the following scale for the hydraulic conductivity

$$G \sim l^4 G'.$$

This results in the following dimensionless formula for the analytic hydraulic conductivity,

$$G = Q. \tag{34}$$

4.1.2 Analytic calculation for $\varepsilon \ll 1$:

Firstly, we calculate the flux, Q,

$$Q = \iint v \,\mathrm{d}T = \int_0^{\frac{1}{2}+\varepsilon}\int_0^{-\sqrt{3}\left(\frac{x}{1+2\varepsilon}-\frac{1}{2}\right)} v \,\mathrm{d}y\,\mathrm{d}x + \int_{-\frac{1}{2}}^{0}\int_0^{\sqrt{3}\left(x+\frac{1}{2}\right)} v \,\mathrm{d}y\,\mathrm{d}x. \tag{35}$$

For the second integral term we need only to expand v as the integral limits do not depend on ε. For the first integral we must expand the integrals as well as v. Expanding the inner integral

$$\begin{aligned}
\int_0^{\frac{1}{2}+\varepsilon}\int_0^{-\sqrt{3}\left(\frac{x}{1+2\varepsilon}-\frac{1}{2}\right)} v \,\mathrm{d}y\,\mathrm{d}x &= \int_0^{\frac{1}{2}+\varepsilon}\left(\int_0^{-\sqrt{3}\left(x-\frac{1}{2}\right)} v\,\mathrm{d}y + \varepsilon (v|_{y=-\sqrt{3}\left(x-\frac{1}{2}\right)})\right)\mathrm{d}x + \mathscr{O}\left(\varepsilon^2\right) \\
&= \int_0^{\frac{1}{2}+\varepsilon}\int_0^{-\sqrt{3}\left(x-\frac{1}{2}\right)} v\,\mathrm{d}y\,\mathrm{d}x + \varepsilon \int_0^{\frac{1}{2}+\varepsilon} \left(v_0+\varepsilon v_1\right)|_{y=-\sqrt{3}\left(x-\frac{1}{2}\right)}\,\mathrm{d}x + \mathscr{O}\left(\varepsilon^2\right) \\
&= \int_0^{\frac{1}{2}+\varepsilon}\int_0^{-\sqrt{3}\left(x-\frac{1}{2}\right)} v\,\mathrm{d}y\,\mathrm{d}x + 0 + \mathscr{O}\left(\varepsilon^2\right)
\end{aligned} \tag{36}$$

since we know that $(v_0|_{y=-\sqrt{3}\left(x-\frac{1}{2}\right)} = 0$. Now, expanding the outer integral (36) becomes

$$\begin{aligned}
\int_0^{\frac{1}{2}+\varepsilon}\int_0^{-\sqrt{3}\left(x-\frac{1}{2}\right)} v\,\mathrm{d}y\,\mathrm{d}x &= \int_0^{\frac{1}{2}}\int_0^{-\sqrt{3}\left(x-\frac{1}{2}\right)} v\,\mathrm{d}y\,\mathrm{d}x + \varepsilon\left(\int_0^{-\sqrt{3}\left(x-\frac{1}{2}\right)} v\,\mathrm{d}y\right|_{x=\frac{1}{2}} + \mathscr{O}\left(\varepsilon^2\right) \\
&= \int_0^{\frac{1}{2}}\int_0^{-\sqrt{3}\left(x-\frac{1}{2}\right)} v\,\mathrm{d}y + \varepsilon(0) + \mathscr{O}\left(\varepsilon^2\right)
\end{aligned} \tag{37}$$

Now, using (36) and (37) we can further expand v to compute the conductivity

$$\begin{aligned}
Q &= \int_0^{\frac{1}{2}}\int_0^{-\sqrt{3}\left(x-\frac{1}{2}\right)} \left(v_0+\varepsilon v_1\right)\mathrm{d}y\,\mathrm{d}x + \int_{-\frac{1}{2}}^{0}\int_0^{\sqrt{3}\left(x+\frac{1}{2}\right)} \left(v_0+\varepsilon v_1\right)\mathrm{d}y\,\mathrm{d}x + \mathscr{O}\left(\varepsilon^2\right) \\
&= \int\int \left(v_0+\varepsilon v_1\right)\mathrm{d}T + \mathscr{O}\left(\varepsilon^2\right) \\
&= \int\int v_0\,\mathrm{d}T + \varepsilon\int\int v_1\,\mathrm{d}T + \mathscr{O}\left(\varepsilon^2\right),
\end{aligned} \tag{38}$$

i.e. on expanding, we see that we integrate over the equilateral triangle boundary. Now, v_0 is given by $v_0 = u_0 W_0$ with u_0, W_0 given by $\frac{1}{2\sqrt{3}}$ and (6a) respectively. Integrating over the non-dimensional triangular area with vertices corresponding to the equilateral triangle as shown in Figure 2 yields,

$$\begin{aligned} Q_0 &= 2\int_0^{\frac{1}{2}} \int_0^{-\sqrt{3}\left(\frac{1}{2}-x\right)} v_0 \,\mathrm{d}y\,\mathrm{d}x \\ &= \frac{\sqrt{3}}{320}. \end{aligned} \tag{39}$$

Now it remains to compute $\iint v_1 \,\mathrm{d}T$. We split the integral as follows;

$$Q_1 = \iint v_1 \,\mathrm{d}T = u_0 \left(\iint_T (W_1 + W_0)\,\mathrm{d}T + \iint_{\hat{T}} \left(4\hat{v_\eta} + 12\hat{v_\xi}\right)\mathrm{d}\hat{T} \right) \tag{40}$$

with the integrals split by coordinate system, given by (24). We first compute the integral over T, which can be done analytically;

$$u_0 \iint_T (W_1 + W_0)\,\mathrm{d}T = \frac{2\sqrt{3}}{320}. \tag{41}$$

For the integral over $\hat{T}$ we first note that the $\hat{v_\eta}$ term will not have a contribution to the hydraulic conductivity due to the symmetry in the integral over η. The integral for ϕ_e in $\hat{v}_\xi$ integrates to zero for each term, except when $n = m$. However, when $n = m$, the B_ξ^{mn} term is zero. Therefore the contribution of the $\hat{v_\xi}$ term to the hydraulic conductivity will also be zero.

Now, combining (38), (39) and (41) we calculate the flux of the perturbed triangle to be

$$Q = \frac{\sqrt{3}}{320}(1 + 2\varepsilon). \tag{42}$$

giving a hydraulic conductivity in the near equilateral triangle, G_E of

$$G_E = \frac{\sqrt{3}}{320}(1 + 2\varepsilon). \tag{43}$$

4.1.3 Analytic calculation for $\varepsilon \gg 1$:

To find the hydraulic conductivity in the infinite wedge domain, G_W, we integrate the velocity, given by (30), over the triangular domain in polar coordinates. This requires rewriting the edge furthest from the wedge angle as a distance, R, from the origin given by,

$$R(\theta) = \frac{\sqrt{3}(\delta + 1)}{\delta(\sin(\alpha(\theta + 1)) + \sqrt{3}\cos(\alpha(\theta + 1)))} \tag{44}$$

leading to the integral

$$G_W = \alpha \int_{-1}^{1} \int_0^{R(\theta)} r v_z \,\mathrm{d}r\,\mathrm{d}\theta, \tag{45}$$

where the additional α is from the change of variable to θ. Substituting α from (29), integrating, and performing an asymptotic expansion in δ leads to,

$$\begin{aligned} G_W =& 1.35 \times 10^{-2}\varepsilon + 2.03 \times 10^{-2} + \\ & 3.38 \times 10^{-3}\varepsilon^{-1} - 1.69 \times 10^{-3}\varepsilon^{-2} + 8.46 \times 10^{-4}\varepsilon^{-3} + \mathcal{O}\left(\varepsilon^{-4}\right) \end{aligned} \tag{46}$$

where we have used that $\delta = \varepsilon^{-1}$.

4.2 Geometric approximations

As mentioned in Section 1, network models often use geometric approximations for the hydraulic conductivity. For example, Al-Gharbi and Blunt [46] assume that the triangular flow is Poiseuille type and equivalent to the flow in a cylinder given by the average of inscribed radius of the triangle and the radius of a circle with the same area as the triangle cross section (which is denoted r_e). This leads to the conductivity, G_{AG}, given by

$$G_{AG} = \frac{\pi}{128}\left(\sqrt{\frac{A_t}{\pi}} + r_{\text{inc}}\right)^4, \tag{47}$$

where the area of the cross section is given by A_t, so that $r_e = \sqrt{\frac{A_t}{\pi}}$. This formula is already in a dimensionless form for comparison.

Similarly, Tørå *et al.* [11] develop a dynamic network model that incorporates a shape factor introduced in the geometric methods developed by Mason and Morrow [69]. The shape factor is given by the following equation, where, as before, A_t denotes the area of the triangle and P_t denotes the perimeter,

$$F = \frac{A_t}{P_t^2}. \tag{48}$$

F is a dimensionless quantity which measures the irregularity of a triangle. F has a maximum value of $\frac{1}{12\sqrt{3}}$, which corresponds to the shape factor for equilateral triangles. Tørå *et al.* [11] define the total area of flow by A_{total},

$$A_{\text{total}} = \frac{r_{\text{inc}}^2}{4F}. \tag{49}$$

As our focus here is on single phase flow, this is the relevant area to consider. However, it is worth noting that Tørå *et al.* [11] have formulae specific to the areas of wetting and non wetting flows, which are used in their multiphase flow simulations. The adapted dimensionless formula for the hydraulic conductivity, G_T, based on the formula of Tørå *et al.* [11] is then given by

$$G_T = \frac{1}{32}\left(\sqrt{\frac{A_{\text{total}}}{\pi}} + r_{\text{inc}}\right)^2 A_{\text{total}}. \tag{50}$$

4.2.1 Geometric method formulae

For the Al–Gharbi and Blunt, as well as the Tørå *et al.* approximations we need to calculate the area of the perturbed triangle and the radius of the inscribed circle. For both of the perturbations we obtain

$$A_t = \frac{\sqrt{3}}{4}(1+\varepsilon). \tag{51}$$

The perimeter, P_t, is given by

$$P_t = 2+\varepsilon+\sqrt{1+\varepsilon+\varepsilon^2}. \tag{52}$$

A relation which holds for triangular tubes, as well as for all regular polygons, is that

$$r_{\text{inc}} = 2\frac{A}{P} = 2FP, \tag{53}$$

using (48) [69]. We can then use (52) to find the relevant expressions for the inscribed radius. These formulae can then be used in (47) and (50) to compute the conductivities.

4.3 **Comparison**

Here we consider a comparison of the approximate and analytical hydraulic conductivities given by (47), (50), (34) and (46) with the numerical value of the hydraulic conductivity (denoted G_n) for various values of ε.

4.3.1 Comparison for $\varepsilon \ll 1$

Figure 10 compares the hydraulic conductivities for the near equilateral triangle. We note that the approximations for G_{AG} and G_T are quite disparate which was one of the motivations for this analysis. We also see that the asymptotic solution (43) agrees most closely to the numerical solution up to $\varepsilon \approx 1.5$. Once ε increases past 1.5, the Al-Gharbi and Blunt formula seems to agree the best but then deviates again (we show this deviation occurs around $\varepsilon = 5$ in Figure 12). We plot the triangles for the cases where $\varepsilon = 1.5$ in Figure 11a and $\varepsilon = 5$ in Figure 11b to give an indication of the difference in the triangle shape.

We also compute the relative error of each of the methods used to compute the hydraulic conductivity, in comparison with the numerical value, in Table 1. As expected the errors for G_E are accurate to $\mathscr{O}\left(\varepsilon^2\right)$.

4.3.2 Comparison for $\varepsilon \gg 1$

In this section we carry out a similar analysis as in section 4.3.1 for the hydraulic conductivity in the wedge. These results are displayed in Figure 13, where we observe that once $\varepsilon \approx 6.5$, the wedge formula outperforms the other two. The relative error of each of these methods in comparison with the numerically computed hydraulic conductivity is shown in Table 2. The accuracy of the asymptotic formula is emphasised in Figure 14, where the agreement between the numerical solution and the wedge solution is emphasised as ε increases. These figures verify that the infinite wedge is a good approximation for the case where there has been a large perturbation to the equilateral triangle.

4.4 Composite Formula for Conductivity

As shown in the results in sections 4.3.1 and 4.3.2, the asymptotic conductivities outperform the geometric formulae in both the small and large ε perturbation to the triangle. There is an intermediate interval of ε where neither asymptotic performance is particularly strong. We propose a linear interpolation between the two asymptotic limits to capture the intermediate interval. This is motivated by the seemingly piecewise linear behaviour we observe in the numerics of each perturbation regime. Furthermore, it allows us to define a single conductivity formula which is more practical for implementation in flow algorithms. In Figure 15 we plot both the small and large perturbation hydraulic conductivities. This plot shows the region where the small perturbation solution begins to diverge, and where the wedge solution begins to converge. We perform a linear interpolation between the two asymptotic conductivities at the point where each has a relative error of 0.1 with the numerical conductivity. This leads to a composite hydraulic conductivity, G_C,

$$G_C = \begin{cases} \frac{\sqrt{3}}{320}(1+2\varepsilon) \text{ for } \varepsilon \leq 1 \\ 1.15\times 10^{-3} + 1.51\times 10^{-1}\varepsilon \text{ for } 1 < \varepsilon < 12.5 \\ 1.35\times 10^{-2}\varepsilon + 2.03\times 10^{-2} + 3.38\times 10^{-3}\varepsilon^{-1} - \\ \ 1.69\times 10^{-3}\varepsilon^{-2} + 8.46\times 10^{-4}\varepsilon^{-3} \text{ for } \varepsilon \geq 12.5. \end{cases} \tag{54}$$

The composite conductivity is plotted in Figure 16. We see that our crude interpolation continues to outperform both geometric approximations and thus (54) is the best approximation for the triangles considered.

4.4.1 Dimensional formulae

In order to carry out the asymptotic analysis we non dimensionalised the problem and then compared the analytical formula with the non dimensional geometric and numerical hydraulic conductivities. For practical use of the composite conductivity formula (54), we will now reintroduce the dimensional scale. The scale for the hydraulic conductivity is l^4, where l is the characteristic length of the equilateral pore. Then, Δl represents how far from equilateral the base of the pore is. From this we get that the dimensional form of (54) is

$$G_C = \begin{cases} \frac{\sqrt{3}l^3}{320}(l+2\Delta l) \text{ for } \Delta l \leq l \\ 1.15\times 10^{-3} l^4 + 1.51\times 10^{-1} l^3 \Delta l \text{ for } l < \Delta l < 12.5l \\ 1.35\times 10^{-2} l^3 \Delta l + 2.03\times 10^{-2} l^4 + 3.38\times 10^{-2} \dfrac{l^5}{\Delta l} - \\ \quad 1.69\times 10^{-2} \dfrac{l^6}{\Delta l^2} + 8.46\times 10^{-3} \dfrac{l^7}{\Delta l^3} \text{ for } \Delta l \geq 12.5l. \end{cases} \tag{55}$$

The dimensional Tørå *et al.* [11] and Al-Gharbi and Blunt [46] formulae also scale with l^4, the dimensional form of these formulae are equivalent to (47) and (50) where this length scale is absorbed into the dimensional area and inscribed radius. Furthermore, we note that there is a relationship between the dimensionless ε and the shape factor, F, given by

$$F := \frac{A}{P^2} = \frac{\sqrt{3}(1+\varepsilon)}{4\left(2+\varepsilon+\sqrt{1+\varepsilon+\varepsilon^2}\right)^2}. \tag{56}$$

Then using (53) we can rewrite (56) in terms of the area and inscribed radius as

$$\frac{r_{\text{inc}}^2}{A} = \frac{\sqrt{3}(1+\varepsilon)}{\left(2+\varepsilon+\sqrt{1+\varepsilon+\varepsilon^2}\right)^2}, \tag{57}$$

therefore giving an alternative expression for ε. We plot the relative error of each of the dimensional formulae with the corresponding numerical hydraulic conductivity for various values of Δl, where we have taken $l = 10\mu$m, in Figure 17.

4.5 Other approximations

There are alternative approaches one could take to determine hydraulic conductivity, here we discuss a couple of particular interest. Other more general rules have been used to compute conductivity, one particular example which we consider for comparative purposes is based on the flow rate for general pipe shapes proposed by Bruus in [70] and [71]. This approximate formula, given by $\mu Q = \frac{\partial p}{\partial z}\frac{A^3}{2P^2}$ is based on a dimensional analysis argument. This formula was investigated by Lekner [72] in the context of a triangular pipe. In this paper Lekner compared this flow formula with the actual flow rate, estimating the ratio of the actual flow to the predicted flow to be ~ 1.2 for a triangular cross section. We carried out a similar analysis using the numerical conductivities and found that the ratio of actual to predicted varied from 1.19 for $\varepsilon = 0.01$ to 1.3 for $\varepsilon = 30$, agreeing with the findings of Lekner [72].

An alternative approach to the perturbative approach taken here is to consider conformal shape perturbations that have exact solutions. This type of approach is outlined in Bazant [66] and is based on de Saint-Venant's velocity solutions for m-sided polygonal domains with rounded edges. Following the approach of Bazant [66] we use the following expression for the exact solution of the velocity profile of a triangular domain with rounded edges

$$u = \frac{1}{4}\left(1 - r^2 + a_m r^m \sin(m\theta)\right). \tag{58}$$

We note that this expression for the velocity will approximately correspond to zero velocity on the boundary of an equilateral triangular domain on taking $m = 3,\ a_m = -0.36$. To consider more scalene triangles we consider an adjustment to the velocity profile adapted from Bazant [66] of the form:

$$u = \frac{1}{4}\left(1 - r^2 + a_m r^m \sin(m\theta) - c_m \frac{1.05 - r\cos(\theta)}{1.05^2 - 2.1 r\cos(\theta) + r^2}\right) \tag{59}$$

When comparing this with the numerical solution in a triangular domain of the same geometry, albeit with straight edges, we considered three cases, equilateral ($c_m = 0$), near equilateral ($c_m = 0.55$) and far from equilateral ($c_m = 1$). The relative errors for the hydraulic conductivity were 0.328, 0.532 and 0.121 respectively. Comparing these errors with the results obtained by our asymptotic approach, shown in Table 1 and Table 2, we see that the asymptotic formula is a more accurate prediction of the hydraulic conductivity. We note that the rounded edges may be a better approximation of real pores, however under the constraint of straight pores the asymptotic approach yields more accurate results. Furthermore, the aim of this work is to provide an improved formula which can be used in the network codes, therefore the formula needs to be easy to implement for many nodes of varying pore size. In this framework we have little control over the precise geometry of the pore.

5 Discussion and Conclusions

The study of flow in porous media is a large and diverse area of research. Since the work carried out by Darcy [73] there have been a number of approaches taken to improve analysis of porous flow. Most importantly, CFD simulations, network models and macroscale models have enabled more accurate modelling of both single phase and multiphase porous media flow.

Network models are becoming increasingly important for modelling flow in porous media due to their ability to incorporate a range of the physically observed phenomena, such as piston displacement, drainage and imbibition. However, network models depend on accurate formulations for determining parameters such as the hydraulic conductivity. The complexity of the network requires low-level computation at each node, making it computationally expensive to numerically solve the flow problem, therefore a more analytic approach is preferable. For this paper we investigated pore-scale models and compared the results obtained for hydraulic conductivity to those used in contemporary network models.

Our approach was to consider both small and large perturbations to the length of one of the sides of an equilateral triangle. Analytical solutions for various cases were obtained and the associated conductivities compared with the results of various approximate methods in the literature. We found that our analytical solutions compare well with the numerics, in particular they compare more favourably than the geometric approximations. In Section 3 we showed that that there is an order of magnitude difference between conductivity results obtained from the approximation methods employed by network models relative to the true values based on numerical results. It appears that the approximations used by Tørå *et al.* [11] coincide with both the numerical and the analytical values more consistently than those of Al-Gharbi and Blunt [46] for small values of ε, but then quickly diverge. The results of Al-Gharbi and Blunt [46] improve as ε increases until the curve intersects the numerical curve, before again diverging. We observe that the Tørå *et al.* [11] formula appears to diverge most quickly in both the small and large perturbation cases, however their full formula was set up with multiphase flow in mind and accounts separately for the wetting and non wetting layers of fluid. This could explain the poor agreement for single phase flow.

It is clear how changes in the perturbation will affect the analytic solution, whereas calculations have to be revised for the approximate methods based on the geometry of the perturbation. This can be seen as an advantage of the asymptotic approach as we have a stronger handle on perturbations than the numerically approximated solutions from the geometric methods. This means that the analytic formulae developed for the hydraulic conductivity allows a large range of triangles to be considered without the need to recompute the flow. For this reason, it would be easy to account for each node in a network having a different sized triangle.

For our formulation we considered the perturbation to the triangle in a particular way, by fixing one side to have length one with an angle of $60°$ to the base and then varying the length of the base. The final side and two angles were then determined through this perturbation. Not all scalene triangles can necessarily be perturbed in this way, such as triangles that have no angles near $60°$. However, this perturbation technique can be explored by changing the angle as well and it is of future interest to see the extent to which the composite conductivity (54) generalizes to arbitrary scalene triangles. With this in mind we note that more delicate consideration must be taken if the wedge angle becomes obtuse [66,74]. Nevertheless, we have demonstrated its power for a broad range of triangles. Furthermore, we note that while not reported, analogous results can be obtained for different triangular orientations. Numerical experiments carried out by Long *et al.* [35] suggest that the hydraulic conductivities do not explicitly depend on the geometry of the pore, but rather the geometric shape factor, F, providing optimism that our formula indeed generalizes. This is an interesting avenue of future research.

This paper placed focus on understanding single phase flow in porous media; however, future work will aim to further extend the work carried out here to multiphase flow. Next steps will involve analysis of the conditions imposed on the meniscus interface between two fluids in the corner of a triangle. Once these are established they can be applied a duct flow analysis in the corner of a triangle to gain insight into the velocity profile and hydraulic conductivities in the limiting case where we have a triangle, almost fully saturated with one fluid, with an $\mathscr{O}(\varepsilon)$ layer of wetting fluid. Having analysed the hydraulic conductivities for this limiting case we will then carry out a comparison with the network approximations. We will then further extend the analysis to various wetting/non-wetting saturation scenarios.

We note that it is insufficient to have only pore-models of the flow, as connections between pores are important features of real porous media as mentioned in Section 1. It will therefore be important to consider a non-uniform cross section channel so that a full three-dimensional flow model can be analysed.

Acknowledgements L.M.K. acknowledges the financial support of Science Foundation Ireland under grant no. SFI/13/IA/1923, the Mathematics Applications Consortium for Science and Industry under grant no. 12/IA/1683, the Carswell Family Foundation, and an NSERC Vanier Canada Graduate scholarship grant no. 434051. I.R.M. acknowledges The Natural Sciences and Engineering Research Council of Canada Discovery Grant 2019-06337.

References

1. G. De Marsily, Quantitative hydrogeology. Tech. rep., Paris School of Mines, Fontainebleau (1986)
2. Y. Mualem, Water resources research **12**, 513 (1976)
3. B.R. Scanlon, R.E. Mace, M.E. Barrett, B. Smith, Journal of hydrology **276**, 137 (2003)
4. A.R. Khaled, K. Vafai, International Journal of Heat and Mass Transfer **46**, 4989 (2003)
5. K. Vafai, *Porous media: applications in biological systems and biotechnology* (CRC Press, 2010)
6. K. Vafai, *Handbook of porous media* (Crc Press, 2015)
7. F. Vermeulen, B. McGee, et al., Journal of Canadian Petroleum Technology **39** (2000)

8. K. Woodruff, D. Miller, Newtown Creek/Greenpoint oil spill study. Tech. rep., Technical report, Lockheed Martin/REAC (2007)
9. L.W. Lake, P.B. Venuto, Oil & Gas Journal **88**(17), 62 (1990)
10. R.N. Anderson, Scientific American **278**(3), 86 (1998)
11. G. Tørå, P.E. Øren, A. Hansen, Transport in porous media **92**(1), 145 (2012)
12. J.M. DallaValle, *Micrometrics: The technology of fine particles* (Pitman, 1948)
13. J. Kozeny, Royal Academy of Science, Vienna, Proc. Class I **136**, 271/306 (1927)
14. C.S. Slichter, The 19th Ann. Rep. US Geophys Survey. p. 304/319 (1899)
15. Smith, W.O., Physics **3**, 139/146 (1932)
16. I. Fatt, H. Dykstra, et al., Journal of Petroleum Technology **3**, 249/256 (1951)
17. J.I. Gates, W.T. Lietz, et al., in *Drilling and production practice* (American Petroleum Institute, 1950)
18. Purcell, W.R., Journal of Petroleum Technology **1**, 39/48 (1949)
19. I. Fatt, et al., OnePetro (1956)
20. M. Sahimi, *Flow and transport in porous media and fractured rock: from classical methods to modern approaches* (John Wiley & Sons, 2011)
21. Z. Gu, M.Z. Bazant, Chemical Engineering Science **196**, 225 (2019)
22. I. Chatzis, F. Dullien, Int. Chem. Eng.;(United States) **25**(1) (1985)
23. D. Wilkinson, J.F. Willemsen, Journal of Physics A: Mathematical and General **16**(14), 3365/3376 (1983)
24. P. Meakin, A.M. Tartakovsky, Reviews of Geophysics **47**(3) (2009)
25. Buckley, S.E. and Leverett, M.C. et al., Transactions of the AIME **146**(01), 107 (1942)
26. S.M. Hassanizadeh, W.G. Gray, Advances in water resources **13**, 169 (1990)
27. C. Manwart, S. Torquato, R. Hilfer, Physical Review E **62**(1), 893 (2000)
28. H. Okabe, M.J. Blunt, Journal of Petroleum Science and Engineering **46**(1-2), 121 (2005)
29. E.W. Washburn, Physical Review **17**(3), 273/283 (1921)
30. S.M. Hassanizadeh, M.A. Celia, H.K. Dahle, Vadose Zone Journal **1**(1), 38 (2002)
31. Beliaev, A.Y. and Hassanizadeh, S.M., Transport in Porous media **43**(3), 487 (2001)
32. R. Hilfer, Physical Review E **73**(1), 016307 (2006)
33. F. Doster, P. Zegeling, R. Hilfer, Physical Review E **81**(3), 036307 (2010)
34. Patzek, T.W. and Kristensen, J.G., Journal of colloid and interface science **236**(2), 305 (2001)
35. L. Long, Y. Li, M. Dong, Transport in Porous Media **115**(1), 79/100 (2016)
36. S. Whitaker, Transport in porous media **1**(1), 3 (1986)
37. M. Panfilov, *Macroscale models of flow through highly heterogeneous porous media*, vol. 16 (Springer Science & Business Media, 2013)
38. F.A. Dullien, *Porous media: fluid transport and pore structure* (Academic press, 2012)
39. Avraam, D.G. and Payatakes, A.C., Journal of Fluid Mechanics **293**, 207 (1995)
40. M.J. Blunt, Current Opinion in Colloid and Interface Science **6**(3), 197/207 (2001)
41. P. Van Marcke, B. Verleye, J. Carmeliet, D. Roose, R. Swennen, Transport in Porous Media **85**(2), 451 (2010)
42. Y. Mehmani, M.T. Balhoff, Pore Scale Geochemical Processes p. 433/459 (2015)
43. C.Y. Xu, Water Resources Management **13**(5), 369 (1999)
44. A. Becker, J. Nemec, The Influence of Climate Change and Climatic Variability on the Hydrologie Regime and Water Resources pp. 431–445 (1987)
45. I. Moyles, B. Wetton, Journal of Engineering Mathematics **90**, 83 (2015)
46. M.S. Al-Gharbi, M.J. Blunt, Physical Review E **71**(1) (2005)
47. H. Dahle, M. Celia, Comput. Geoscience (1999)
48. C.Z. Qin, H. van Brummelen, Advances in Water Resources **133**, 103420 (2019)
49. J. Boussinesq, J. Math. Pures Appl **13**, 377/424 (1868)
50. J. Proudman, The London, Edinburgh, and Dublin Philosophical Magazine and Journal of Science **28**, 30/36 (1914)
51. E.M. Sparrow, AIChE Journal **8**(5), 599/604 (1962)
52. A. Tamayol, M. Bahrami, Journal of Fluids Engineering **132**(11), 111/201 (2010). DOI 10.1115/1.4001973
53. Shah, R.K., International Journal of Heat and Mass Transfer **18**(7-8), 849 (1975)
54. S. Navardi, S. Bhattacharya, M. Azese, Journal of Engineering Mathematics **99**(1), 103 (2016)
55. R.K. Shah, A.L. London, *Laminar flow forced convection in ducts: a source book for compact heat exchanger analytical data* (Academic press, 2014)
56. R. Kumar, A. Kumar, et al., Renewable and Sustainable Energy Reviews **61**, 123 (2016)
57. P. Jia, M. Dong, L. Dai, J. Yao, Transport in Porous Media **74**(2), 153/167 (2007)

58. H. Nakamura, S. Hiraoka, I. Yamada, Heat Transfer—Japanese Research **1**, 120 (1972)
59. Abdel-Wahed, R.M. and Attia, A.E., Wärme-und Stoffübertragung **18**(2), 83 (1984)
60. J. Lekner, Prediction of Formability in Perovskite-Type Oxides **2**(1) (2009)
61. J. Lekner, European Journal of Physics **28**(3), 521/527 (2007)
62. N. Kurt, M. Sezer, Applied Mathematics and Computation **182**, 73–81 (2006)
63. L.N. Trefethen, R.J. Williams, Journal of Computational and Applied Mathematics **14**(1-2), 227 (1986)
64. M.A. Pinsky, SIAM Journal on Mathematical Analysis **16**(4), 848/851 (1985)
65. B.J. McCartin, SIAM Review **45**(2), 267/287 (2003)
66. M.Z. Bazant, Physical Review Fluids **1** (2016)
67. wikiHow. How to measure water pressure. `https://www.wikihow.com/Measure-Water-Pressure` (2019)
68. S. Bryant, M. Blunt, Physical Review A **46**(4), 2004/2011 (1992)
69. G. Mason, N.R. Morrow, Journal of Colloid and Interface Science **141**(1), 262/274 (1991)
70. H. Bruus, *Theoretical microfluidics*, vol. 18 (Oxford university press Oxford, 2008)
71. H. Bruus, Lab on a Chip **11**(22), 3742 (2011)
72. J. Lekner, American Journal of Physics **87**(10), 791 (2019)
73. H. Darcy, *Les fontaines publiques de la ville de Dijon* (Victor Dalmont, 1856)
74. Moffatt, H.K. and Duffy, B.R., J. Fluid Mech **96**(2), 299 (1980)

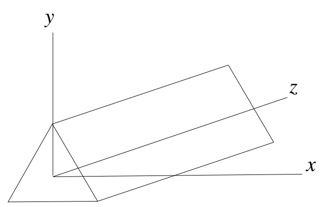

Fig. 1: Diagram depicting how we align the pipe and the direction of flow.

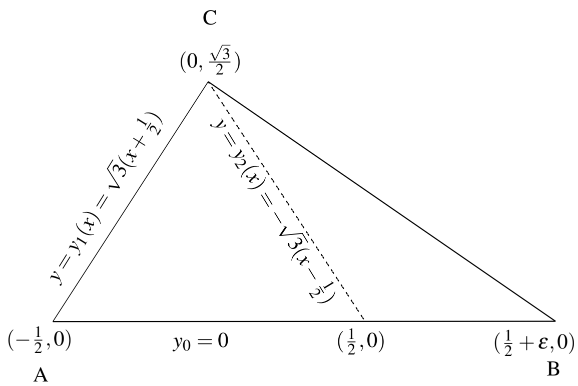

Fig. 2: Perturbed equilateral triangle domain

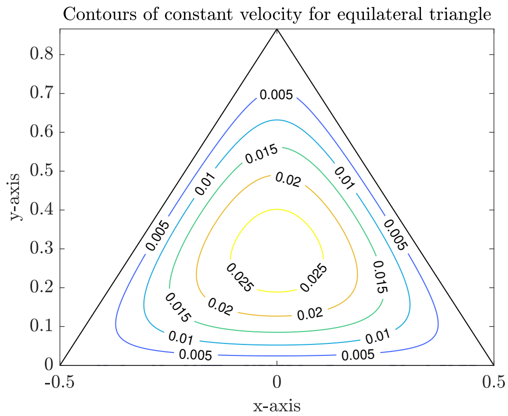

Fig. 3: Contours of constant velocity for the non-dimensional equilateral triangle domain corresponding to Figure 2, where we denote the triangle boundary (given by (6a)) with 0 velocity in black and the velocity profile is given by $v_0 = u_0 W_0$.

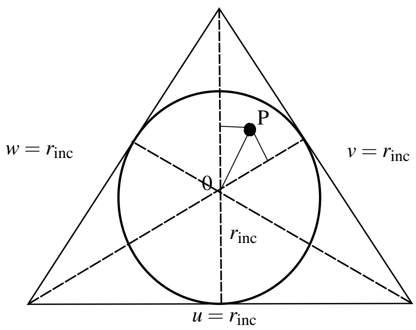

Fig. 4: Triangular coordinate system

Table 1: Relative errors of each of the hydraulic conductivity methods in comparison with the numerical hydraulic conductivity G_n.

Relative errors of the hydraulic conductivities				
ε	Shape factor	G_E	G_{AG}	G_T
0.01	0.04811	3.2781×10^{-5}	1.3987×10^{-1}	8.8897×10^{-2}
0.1	0.04789	4.2160×10^{-3}	1.3985×10^{-1}	9.1059×10^{-2}
0.5	0.04444	4.6331×10^{-2}	1.3845×10^{-1}	1.2873×10^{-1}
1	0.03868	8.8038×10^{-2}	1.3100×10^{-1}	2.0682×10^{-1}
1.5	0.03356	1.1381×10^{-1}	1.1714×10^{-1}	2.9806×10^{-1}
2	0.02941	1.3048×10^{-1}	9.8679×10^{-2}	3.9441×10^{-1}

A Separation of Variables in Triangular Coordinates

Consider the eigenvalue problem

$$\nabla^2 \phi = -\lambda^2 \phi \quad \text{with} \;\; \phi = 0 \;\; \text{on} \;\; W = 0, \tag{60}$$

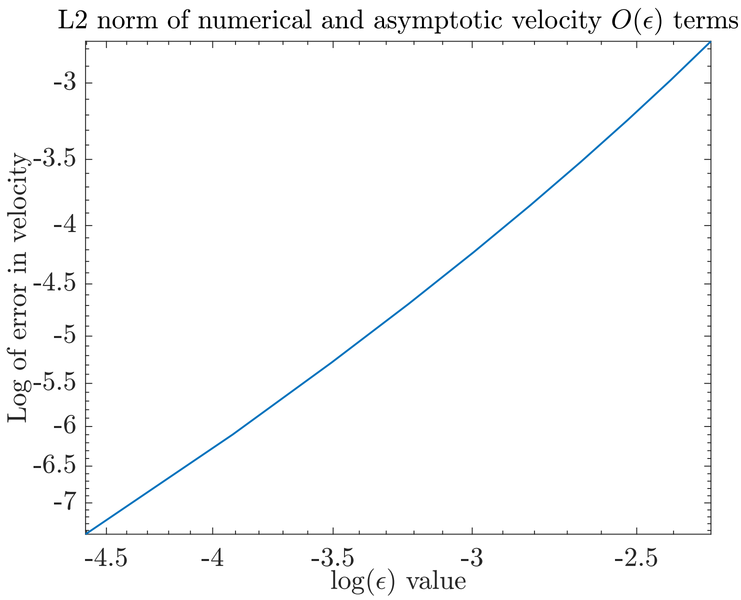

Fig. 5: Log-log plot depicting the $L2$ norm between the analytical and numerical solutions minus the components of the solution involving u_0, W_0, W_1 terms, where $u_0 = \frac{1}{2\sqrt{3}}$, and W_0, W_1 given by (6a) and (6b) respectively. Error decreases at a rate proportional to ε^2 as $\varepsilon \to 0$.

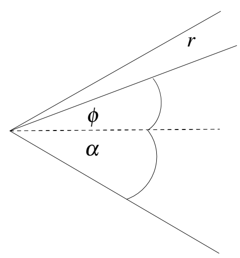

Fig. 6: Isosceles triangular duct cross section

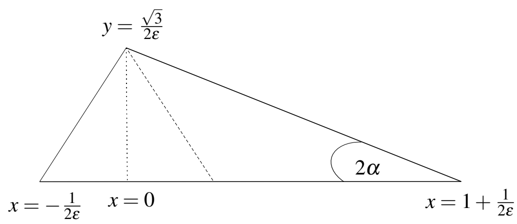

Fig. 7: Rescaled large triangle

where W is the equilateral triangle domain given as in Figure 18.

The problem with separation of variables in this domain is that the boundaries of the triangle are not constant in x or y. Transforming to a triangular coordinate system is useful as each point in space is measured relative

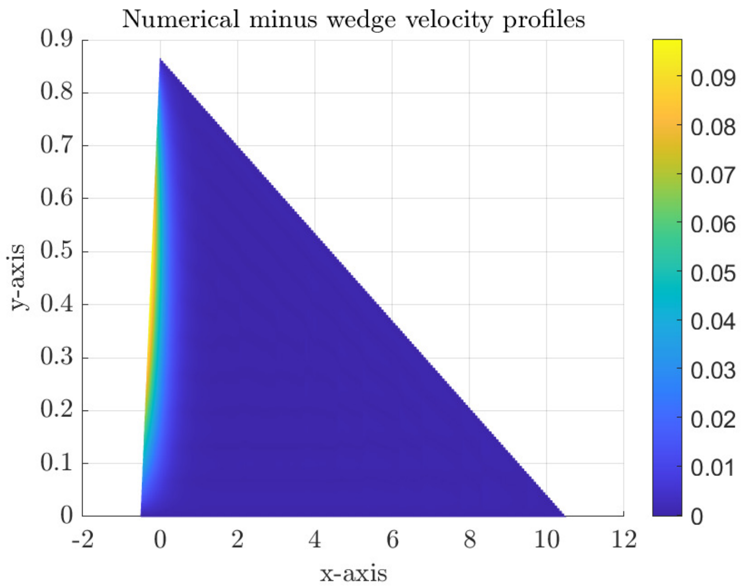

Fig. 8: The absolute value of the numerical velocity for large triangle when $\varepsilon = 10$ with the infinite wedge asymptotic solution subtracted away.

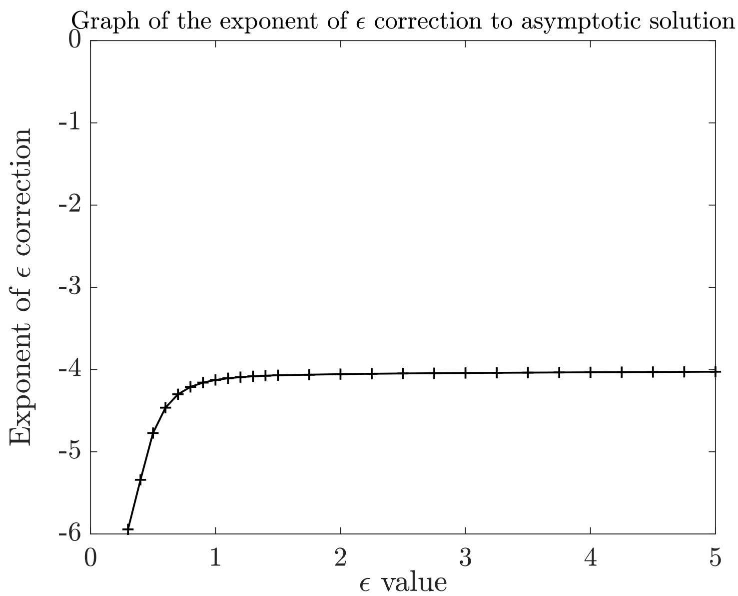

Fig. 9: Convergence of the asymptotic correction term (30) to $\mathcal{O}(\varepsilon^{-4})$, $1 < \varepsilon < 10$. As ε increases the asymptotics approximate the large triangle to $\mathcal{O}(\varepsilon^{-4})$ as predicted.

to the bisectors of the angles through the midpoint of the opposite sides, with the origin being the centre of the inscribed circle of the triangle, with radius $r_{\text{inc}} = \frac{\sqrt{3}}{6}$.

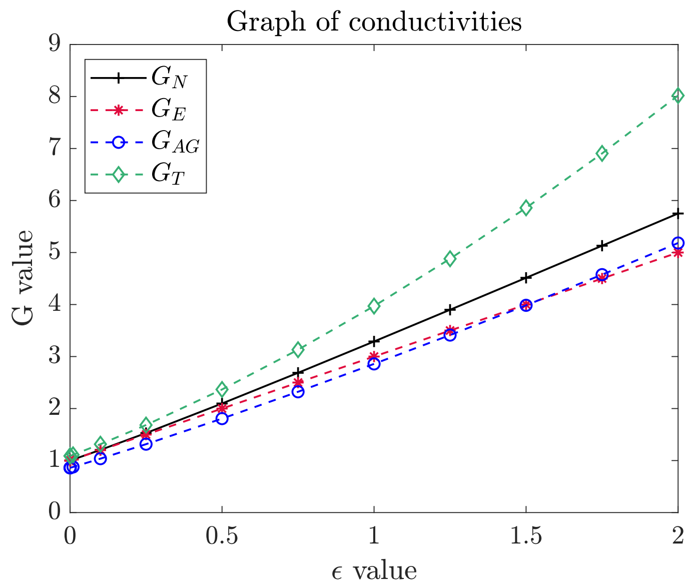

Fig. 10: Comparison of the analytical hydraulic conductivity, G_E, the two approximate methods, G_{AG}, G_T, and the numerical solution, G_N. We scale each G by the leading order conductivity $\frac{\sqrt{3}}{320}$ in order to present $\mathscr{O}(1)$ conductivities.

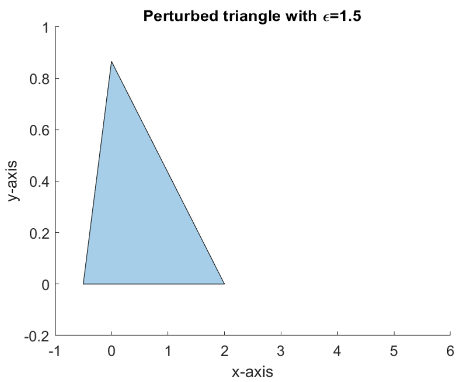

(a) $\varepsilon = 1.5$, Shape Factor= 0.03356

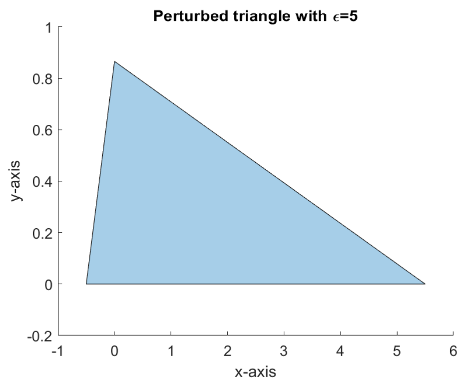

(b) $\varepsilon = 5$, Shape Factor= 0.01645

Fig. 11: Perturbed triangles for different ε values.

Considering Figure 19, each point P in (x,y,z) is projected onto (u,v,w) in this new coordinate system, giving the following relations

$$u = r_{\text{inc}} - y \tag{61a}$$

$$v = \frac{\sqrt{3}}{2}x + \frac{1}{2}(y - r_{\text{inc}}) \tag{61b}$$

$$w = -\frac{\sqrt{3}}{2}x + \frac{1}{2}(y - r_{\text{inc}}) \tag{61c}$$

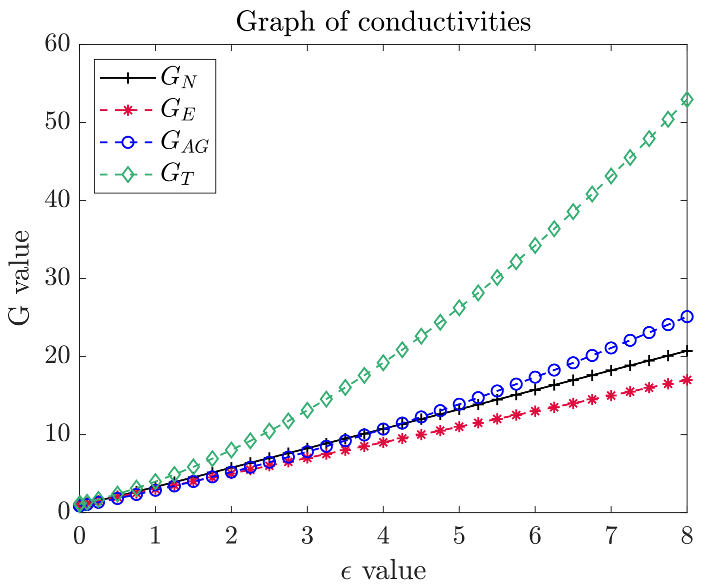

Fig. 12: Graph showing the comparison of the analytical hydraulic conductivities, the two approximate methods and the numerical solution using the figures from Table 1 and larger values of ε. Each G is scaled by the leading order conductivity $\frac{\sqrt{3}}{320}$ in order to present $\mathscr{O}(1)$ conductivities.

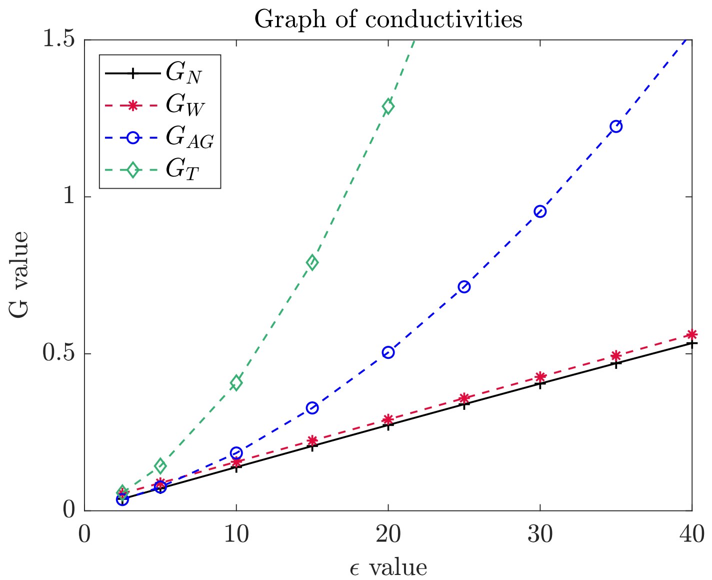

Fig. 13: Hydraulic conductivities for large perturbation to the equilateral triangle with $2.5 < \varepsilon < 40$.

with positive orientation directed towards the boundary. Adding these three equations it can be seen that there is a linear dependence in the variables,

$$u + v + w = 0, \tag{62}$$

which is consistent with $\mathbb{R}^2$ being uniquely spanned by two vectors. Now, in this new coordinate system, the boundaries of the triangle are now $u = r_{\text{inc}}$, $v = r_{\text{inc}}$ and $w = r_{\text{inc}}$, which are constant values and so allow us to proceed with separation of variables.

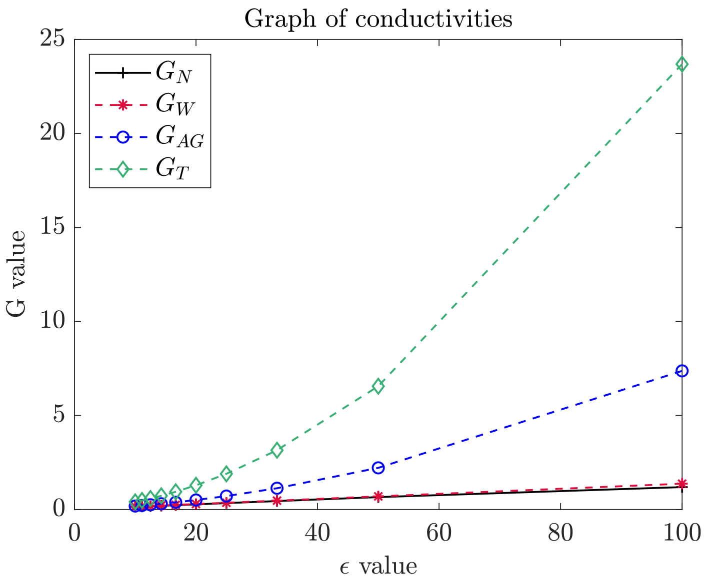

Fig. 14: Hydraulic conductivities for large perturbation to the equilateral triangle with $10 < \varepsilon < 100$.

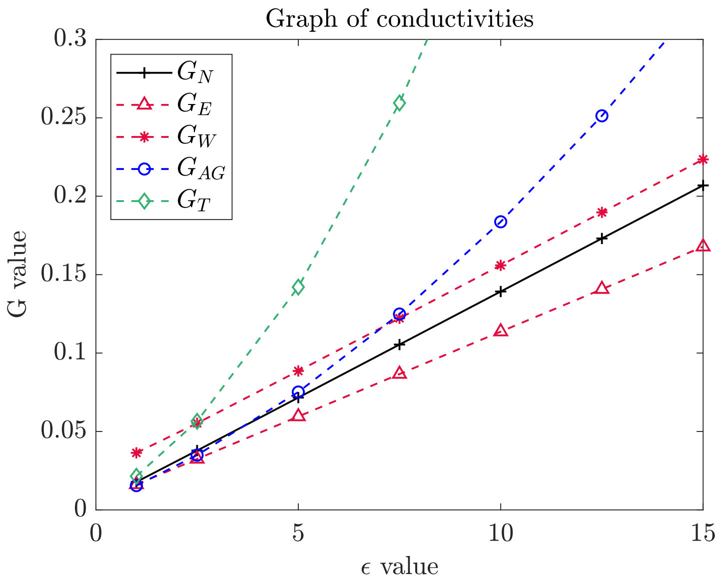

Fig. 15: Hydraulic conductivities for various ε values demonstrating the regions where the small and large perturbation formulae overlap in performance.

Rearranging the equations in (61) we see that

$$x = \frac{v - w}{\sqrt{3}} \tag{63a}$$

$$y = r_{\text{inc}} - u \tag{63b}$$

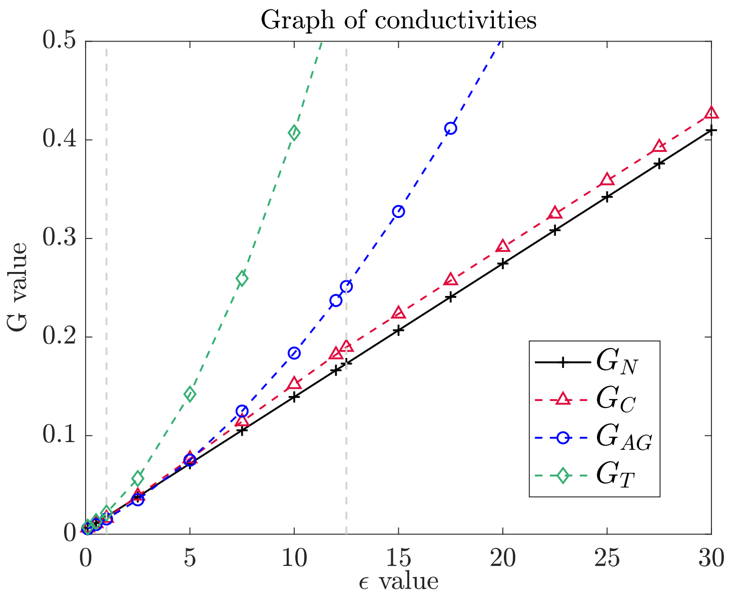

Fig. 16: Hydraulic conductivities for various ε values demonstrating the complete analytic conductivity formula, G_C given by (54), in comparison with the two geometric formulae and the numerical conductivity. The grey dashed lines denote the points where the line fit meets the two asymptotic formulae.

Table 2: Relative errors of each of the hydraulic conductivity methods in comparison with the numerical hydraulic conductivity G_n for $\varepsilon \gg 1$.

Relative errors of the hydraulic conductivities				
ε	Shape factor	G_W	G_{AG}	G_T
2.5	0.026943	4.6017×10^{-1}	5.4998×10^{-2}	5.1060×10^{-1}
5	0.016627	2.3724×10^{-1}	5.6999×10^{-2}	9.9136×10^{-1}
10	0.009409	1.2130×10^{-1}	3.2314×10^{-1}	1.9307
15	0.006559	8.3342×10^{-2}	5.8795×10^{-1}	2.8342
20	0.005034	6.5793×10^{-2}	8.4702×10^{-1}	3.7169
25	0.004085	5.6820×10^{-2}	1.1018	4.5882
30	0.003436	5.2610×10^{-2}	1.3542	5.4552

and so defining $\xi = u$ and $\eta = v - w$ provides a good orthogonal system. In this new coordinate system the Laplace operator can be written as

$$\nabla^2 = \frac{\partial^2}{\partial x^2} + \frac{\partial^2}{\partial y^2} = \frac{\partial^2}{\partial \xi^2} + 3\frac{\partial^2}{\partial \eta^2} = \hat{\nabla}^2, \tag{64}$$

and the system (60) becomes

$$\hat{\nabla}^2 \phi = -\lambda^2 \phi, \tag{65}$$

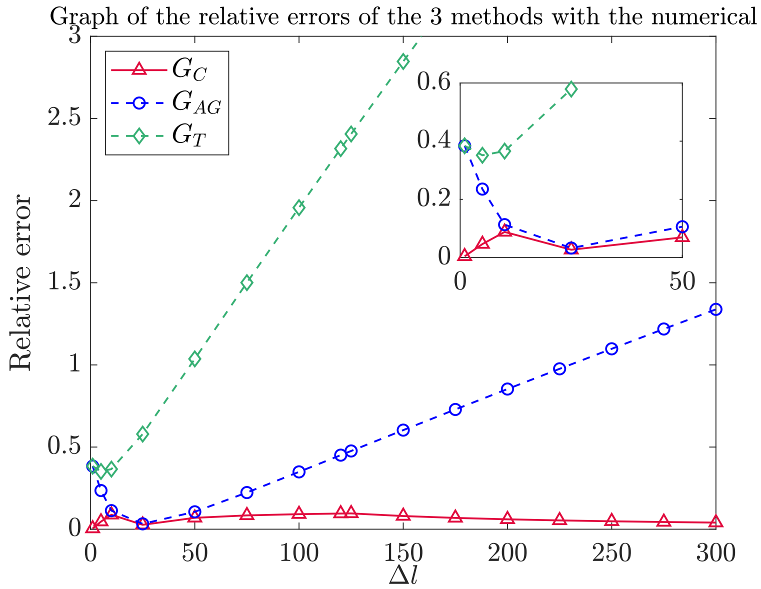

Fig. 17: Relative error of hydraulic conductivities for various Δl values where $l = 10\mu$m. the inset plot zooms in on the area where the error of G_{AG} is close to the error of G_C.

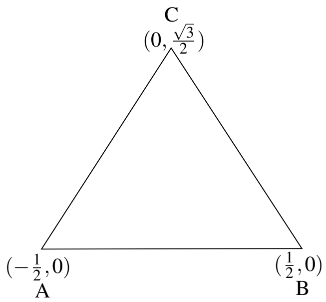

Fig. 18: Equilateral triangle domain

subject to $\phi = 0$ on $\xi = r_{\text{inc}}$, $\eta = u + 2r_{\text{inc}}$, and $\eta = -u - 2r_{\text{inc}}$. Seeking a separable solution of the form $\phi(\xi, \eta) = f(\xi)g(\eta)$ and substituting this into (65) yields

$$f_{\xi\xi} + \alpha^2 f = 0 \tag{66a}$$

$$g_{\eta\eta} + \beta^2 g = 0 \tag{66b}$$

$$\alpha^2 + 3\beta^2 = \lambda^2. \tag{66c}$$

Solutions to (66a) and (66b) are simple harmonic oscillators. We first consider the solution to (66a). The boundary condition to be satisfied is $\phi = 0$ on $\xi = r_{\text{inc}}$, but we need a second boundary condition. Considering that we would like the top corner of the triangle to be consistent with the boundary conditions on the triangle sides, we impose that $\phi = 0$ on $\xi = -2r_{\text{inc}}$. Thus, we require $f(r_{\text{inc}}) = f(-2r_{\text{inc}}) = 0$. Let's consider a shift in $f(\xi)$,

$$f(\xi) = \cos\alpha(\xi - \gamma) + \sin\alpha(\xi - \gamma), \tag{67}$$

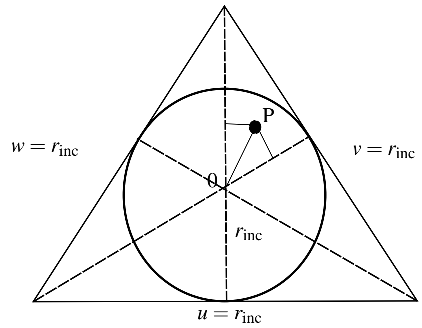

Fig. 19: Triangular coordinate system

for some constant γ. Taking $\gamma = -2r_{\text{inc}}$ we see that

$$f(\xi) = \sin\left(\frac{l\pi}{3r_{\text{inc}}}(\xi + 2r_{\text{inc}})\right), \quad l \in \mathbb{N},\ l \neq 0; \quad \alpha = \frac{l\pi}{3r_{\text{inc}}}. \tag{68}$$

In order to solve the original problem we will consider separately the even and odd functions of η, denoted ϕ_e and ϕ_o respectively,

$$\phi_e = \sin\left(\frac{l\pi}{3r_{\text{inc}}}(\xi + 2r_{\text{inc}})\right)\cos(\beta\eta) \tag{69a}$$

$$\phi_o = \sin\left(\frac{l\pi}{3r_{\text{inc}}}(\xi + 2r_{\text{inc}})\right)\sin(\beta\eta), \tag{69b}$$

noting that if both ϕ_e and ϕ_o satisfy (60) then their sum will automatically satisfy (60) also. Now we must satisfy the boundary conditions at $v = r_{\text{inc}}$ and $w = r_{\text{inc}}$, which are equivalent to $\eta = u + 2r_{\text{inc}}$ and $\eta = -u - 2r_{\text{inc}}$. By symmetry, if $\phi = 0$ is satisfied at one of these two boundaries, then it is satisfied at the other also.

Considering ϕ_e, we need to satisfy $\phi_e = 0$ at $\eta = u + 2r_{\text{inc}}$. Recall that $\xi = u$,

$$\phi_e = \sin\left(\frac{l\pi}{3r_{\text{inc}}}(u + 2r_{\text{inc}})\right)\cos\Big(\beta(u + 2r_{\text{inc}})\Big) = 0. \tag{70}$$

Now (70) cannot be zero for all u. But we know that ϕ_e is a solution for all non-zero integers. This then motivates consideration of additive solutions at $\eta = u + 2r_{\text{inc}}$ of the form

$$\phi_e = \sin\left(\frac{l\pi}{3r_{\text{inc}}}(u + 2r_{\text{inc}})\right)\cos\Big(\beta_l(u + 2r_{\text{inc}})\Big) + \sin\left(\frac{m\pi}{3r_{\text{inc}}}(u + 2r_{\text{inc}})\right)\cos\Big(\beta_m(u + 2r_{\text{inc}})\Big) = 0. \tag{71}$$

Trigonometric identities can be used to write (71) as a sum of sines, which then indicates that for $\phi_e = 0$ to be satisfied we have $\phi_e = 0$, so the two mode solution is also inadequate. We consider adding more integers,

$$\begin{aligned}\phi_e = \sin\left(\frac{l\pi}{3r_{\text{inc}}}(u + 2r_{\text{inc}})\right)\cos\Big(\beta_l(u + 2r_{\text{inc}})\Big) + \sin\left(\frac{m\pi}{3r_{\text{inc}}}(u + 2r_{\text{inc}})\right)\cos\Big(\beta_m(u + 2r_{\text{inc}})\Big)\\ + \sin\left(\frac{n\pi}{3r_{\text{inc}}}(u + 2r_{\text{inc}})\right)\cos\Big(\beta_n(u + 2r_{\text{inc}})\Big) = 0.\end{aligned} \tag{72}$$

Writing (72) as a sum of sines, it can then be seen that $\phi_e = 0$ if

$$\frac{l\pi}{3r_{\text{inc}}} - \beta_l = -\frac{m\pi}{3r_{\text{inc}}} - \beta_m, \tag{73a}$$

$$\frac{l\pi}{3r_{\text{inc}}} + \beta_l = -\frac{n\pi}{3r_{\text{inc}}} + \beta_n, \tag{73b}$$

$$\frac{m\pi}{3r_{\text{inc}}} - \beta_m = -\frac{n\pi}{3r_{\text{inc}}} - \beta_n, \tag{73c}$$

where it should be noted that these choices are not unique. We notice that adding the above expressions

$$l+m+n=0, \tag{74}$$

which echoes the linear dependence $u+v+w=0$. Adding (73a) and (73c), substituting m based on (74) we see

$$\beta_n-\beta_l=\frac{(l+n)\pi}{3r_{\text{inc}}}. \tag{75}$$

Then, due to the degeneracy in (74), we recall the condition (66c), which simplifies as

$$\beta_l^2-\beta_n^2=\frac{(n^2-l^2)\pi^2}{27r_{\text{inc}}^2}. \tag{76}$$

Combining (75) and (76) we can solve for β_n, and then we can use (73) to determine β_l and β_m,

$$\beta_n=\frac{(l-m)\pi}{9r_{\text{inc}}}, \tag{77a}$$

$$\beta_l=\frac{(m-n)\pi}{9r_{\text{inc}}}, \tag{77b}$$

$$\beta_m=\frac{(n-l)\pi}{9r_{\text{inc}}}, \tag{77c}$$

with corresponding eigenvalue,

$$\lambda_{mn}^2=\frac{4\pi^2}{27r_{\text{inc}}^2}(m^2+mn+n^2). \tag{78}$$

The odd solution ϕ_o can be determined in a similar manner, where, in fact, due to the choice of conditions in (73), we find that the odd solution is of the same form. Thus the solution to (65) subject to the homogeneous Dirichlet boundary conditions is given by

$$\begin{aligned}\phi_e^{mn}&=\sin\left(\frac{l\pi}{3r_{\text{inc}}}(\xi+2r_{\text{inc}})\right)\cos\left(\frac{(m-n)\pi}{9r_{\text{inc}}}\eta\right)+\sin\left(\frac{m\pi}{3r_{\text{inc}}}(\xi+2r_{\text{inc}})\right)\cos\left(\frac{(n-l)\pi}{9r_{\text{inc}}}\eta\right)\\&\quad+\sin\left(\frac{n\pi}{3r_{\text{inc}}}(\xi+2r_{\text{inc}})\right)\cos\left(\frac{(l-m)\pi}{9r_{\text{inc}}}\eta\right)=0, \qquad (79a)\\\phi_o^{mn}&=\sin\left(\frac{l\pi}{3r_{\text{inc}}}(\xi+2r_{\text{inc}})\right)\sin\left(\frac{(m-n)\pi}{9r_{\text{inc}}}\eta\right)+\sin\left(\frac{m\pi}{3r_{\text{inc}}}(\xi+2r_{\text{inc}})\right)\sin\left(\frac{(n-l)\pi}{9r_{\text{inc}}}\eta\right)\\&\quad+\sin\left(\frac{n\pi}{3r_{\text{inc}}}(\xi+2r_{\text{inc}})\right)\sin\left(\frac{(l-m)\pi}{9r_{\text{inc}}}\eta\right)=0. \qquad (79b)\end{aligned}$$

More detail can be found in McCartin [65].